

Article

Atomistic Simulations of Defect Structures in Rare-Earth-Doped Magnesium Oxide

Yanfeng Zhao, Alastair N. Cormack * and Yiquan Wu

Kazuo Inamori School of Engineering, New York State College of Ceramics, Alfred University, Alfred, NY 14802, USA; yz8@alfred.edu (Y.Z.); wuy@alfred.edu (Y.W.)

* Correspondence: cormack@alfred.edu

Abstract: Point defects induced by doping rare earth elements (RE) (Nd and Er) into a magnesium oxide host were investigated via classical atomistic simulations utilising the General Utility Lattice Program (GULP). Formation and association energies were calculated for the potential defect structures. Both isolated defects and defect complexes were considered. The most energetically favourable structures of defect complexes were found for rare-earth-doped and Li co-doped systems. The correlation between the association energy and the structure of the defect complex was investigated. The influences of Li were revealed with respect to energy and structure. The simulation results contribute to the understanding of the point defects of doped MgO and how Li influences the doping of rare earth elements in the MgO host.

Keywords: atomistic simulation; point defect; defect structure; rare earth dopant; magnesium oxide



Citation: Zhao, Y.; Cormack, A.N.; Wu, Y. Atomistic Simulations of Defect Structures in Rare-Earth-Doped Magnesium Oxide. *Crystals* **2024**, *14*, 384. <https://doi.org/10.3390/cryst14040384>

Academic Editor: Nikos Ch. Karayiannis

Received: 26 March 2024

Revised: 11 April 2024

Accepted: 13 April 2024

Published: 19 April 2024



Copyright: © 2024 by the authors. Licensee MDPI, Basel, Switzerland. This article is an open access article distributed under the terms and conditions of the Creative Commons Attribution (CC BY) license (<https://creativecommons.org/licenses/by/4.0/>).

1. Introduction

Because of its highly symmetric crystal structure, magnesium oxide (MgO) has long been recognized as an important model ceramic material that has found application in a wide range of technologies such as electronics, catalysis, and medicine.

More recently, it has been investigated as a potential host for optical applications. Its cubic symmetry provides a potentially useful site for optically active ions such as the rare earths [1–8].

However, there are practical challenges to producing single crystals of MgO doped with sufficient concentrations of the rare earth dopants. The success in producing transparent polycrystalline MgO opened the possibility of using this ceramic as the host and, hence, as an alternative to the popular Nd-doped YAG laser material. Largely, this is because the development of ‘soft’ chemical routes, which start from the mixing of chemical solution precursors (of host and dopant species), has gained popularity for synthesizing rare-earth-doped MgO ceramics, in contrast to traditional solid-state routes. The benefits include tighter control over the chemistry and considerable energy savings because of the lower temperatures used.

A further advancement was the discovery that co-doping with lithium contributed positively to the optical properties of oxide materials doped with rare earth ions. Orante-Barrn [9] investigated Ce³⁺ doped MgO with Li as a co-dopant. The undoped and doped MgO ceramic powder samples were both prepared using the solution combustion method (SCM). Li was found to improve the luminescence intensities significantly. Li’s substitution on the Mg cation site was indicated as an essential factor that induced the improvement in optical performance, but the detailed defect structures accommodating the dopant and co-dopant incorporation and their formation mechanisms remained unclear.

Feng Gu [10] synthesized Eu:MgO nanocrystals in the form of powders using the SCM, and the photoluminescence intensity and crystallinity were enhanced after introducing Li as a co-dopant. Sivasankari [11] studied alkali co-doped (Na, K, and Li) Er: MgO. Their nanopowder samples were synthesised using the SCM as well. The sample with the Li

co-dopant was found to have smaller FWHM (Full Width at Half Maximum) values, with peak profile changes in the X-ray diffraction pattern, indicating that the crystallinity was improved. Crisan et al. [12] tried to synthesise $\text{Nd}_2\text{O}_3\text{-MgO}$ two-phase systems in the form of ceramic powders using the chemical sol–gel method. Calculations on the mass of unit cell showed that almost no change was observed in the MgO host when introducing Nd_2O_3 as the impurity, meaning there was no ionic exchange. It was suggested that vacancies and ionic exchange reactions compete within the unit cell. Whether they were cation or anion vacancies or specific ionic substitutions was not clarified. Nevertheless, it indeed indicated a particular difficulty for doping Nd into MgO. According to Oliveira [6], Li improves luminescence intensities in Nd:MgO. The doped ceramic powder samples were prepared using the SCM. It was proposed that Li may provide charge compensation for neighbouring Nd. However, it was not clear how the proposed role of Li accounts for the change in the optical emissions of Nd in the sample. Nd:MgO and Er:MgO transparent ceramics were investigated by Sanamyan [13] for potential laser applications. Li was used as a co-dopant. The bulk-doped ceramic samples were fabricated via hot isostatic pressure (HIP) steps. Li was found to be directly beneficial for dopants to enter the host. And, Er, Li:MgO was found to exhibit better visible transparency than Nd, Li:MgO.

But, some unsolved problems impede the development of rare-earth-doped optical crystalline materials, such as luminescence quenching, complexities arising from co-doping, and effects of doping on thermal and mechanical properties. The introduction of dopants and co-dopants initiates the formation of point defects within the host material. However, our understanding and insight into the energetics and the defect structures of the rare earth dopants and co-dopants in the host are still limited. Thus, relevant investigations are pressingly necessary.

Due to the difficulties and complexities of characterizing defects in materials at the atomic scale, using atomistic simulations, a well-established tool from a theoretical basis that will enable us to investigate defects at atomic scale, is necessary. Because of its position as an archetype (or model) material, MgO has been the subject of many studies, employing a variety of simulation methodologies, as listed in Table 1.

Table 1. Topics about MgO investigated via simulations.

Topic Investigated		Reference
Intrinsic point defects and diffusion		[14–20]
Impurity/dopant	Alkali metal trapped hole $[\text{Li}]^0$	[21–23]
	Fluorine F^{-1}	[24]
	S^{2-} and Se^{2-}	[25]
	Li, Al, Ti, Fe, Cu, Zn, Ag	[26]
Dislocations/grain boundaries/surfaces/interfaces		[27–30]
Radiation damage		[31,32]
Melting and phase diagram		[33–35]
Low energy recoil events		[36]

For example, Karki and Khanduja [14] investigated the effects of pressure on the energetics of intrinsic magnesium and oxygen vacancies in MgO using density functional theory (DFT) within the local density approximation (LDA). The density of states of MgO containing intrinsic magnesium and oxygen vacancies were calculated by Gao et al. [15] using DFT within LDA. Ertekin et al. [19] calculated the ionization energies of F-centres in MgO using quantum Monte Carlo methods. Linear and planar defects, such as dislocations, grain boundaries, and interfaces, have also been studied through simulations using molecular dynamics [27] and DFT [28]. Impurities or dopants that have been theoretically studied

include the [Li]⁰ centre [21–23], Fluorine F[−] point defect [24], and other non-lanthanide elements [25,26].

Point defects, both intrinsic and extrinsic, have been the primary research focus of the simulations, but there is lack of pertinent research on the topic regarding the defect chemistry of rare earth elements in crystalline MgO.

Nd and Er are currently of interest as optically active dopants in MgO due to their potential laser applications in the near and mid-infrared spectral regions [13], both possessing a valence state of 3+ under ambient conditions. Optical emissions from rare earth elements arise from electronic transitions between the degenerate 4f manifolds. Nd³⁺ (4f³) and Er³⁺ (4f¹¹) ions possess the same ground state spectral term ⁴I, where I is the orbital angular momentum and the superscript 4 is the spin angular momentum. The reduction of degeneracies to Stark levels depends on the crystal field surrounding the dopant. Defects within the host material exert a profound influence on the symmetry and the strength of the crystal field, directly impacting the optical properties of the rare-earth-doped laser materials.

Due to the much larger ionic radius of the rare earth elements compared to Mg, their solubilities in MgO are negligibly low [13], indicating the difficulty in incorporating them into the MgO host. Theoretical calculations of the energetics of defects are a means of quantifying this difficulty and providing guidance for experimental practice. Insights into defects at the atomistic level in rare-earth-doped crystalline MgO, along with the mechanisms of co-doping Li, are imperative for advancing the field of solid-state laser materials and developing novel experimental approaches to obtain samples with tailored optical properties. This study is driven by the need to uncover the most energetically favourable point defects and defect structures induced by doping rare earth elements (Nd and Er) into the MgO host, while revealing the underlying mechanisms of Li through atomistic simulations.

In this paper, a systematic investigation of point defects and defect complexes was approached primarily for Nd:MgO and Nd, Li:MgO. A comparison with Er:MgO and Er, Li:MgO was conducted. The goal is to uncover the most energetically favourable point defects and defect complexes induced by doping the rare earth elements Nd and Er into the MgO host as well as to elucidate the role of the Li co-dopant in improving the optical properties.

2. Simulation Methodology

The program employed for current simulations is the General Utility Lattice Program (version GULP 4.2), which is based on classical force field methods. The original code of this program was designed for the fitting of interaction potentials to experimental data or energy surfaces. Up-to-date, comprehensive expansions enable it to be a general code for modelling condensed materials, solids (especially ionic materials), clusters, embedded defects, and so on [37]. As for current simulations, the static lattice method [38] has been the primary simulation methodology applied and this is outlined below.

In the static lattice method, interactions between atoms are modelled via a series of functions with unique parameters, depending on the nature of interactions between the different atoms. An approximation in classical static/dynamical lattice theory is pairwise additivity. That is, in a system containing two or more atoms, the energy of the system can be described by the interaction of pairs: summation of two body interactions [39]. In principle, the energy of a many-body system consists of two-body interactions, three-body interactions, four-body interactions, and so on. But, the two-body interactions (long range Coulombic interaction and short-range interactions) have the largest contributions to the total energy of the system. Therefore, under the pairwise additivity approximation, the energy of a many-body system can be expressed as:

$$E_{ij} = \frac{1}{2} \sum_{ij} \varphi_{ij}(r_{ij}). \quad (1)$$

where $\varphi_{ij}(r_{ij})$ is the two-body interaction as a function of the distance between ions. For materials that are considered purely ionic, the lattice energy calculations contain both long-range and short-range interactions, namely, the electrostatic interaction (Coulomb term), the London interaction, which is also known as Van Der Waals (or called dispersion interaction, for historical reasons); and a repulsion term considering Pauli exclusion rules from the effects of overlapping electron densities. The lattice energy expressed by these three two-body interactions is:

$$E_{\text{Lattice}} = \varphi_{\text{Coulomb}} + \varphi_{\text{Repulsion}} + \varphi_{\text{London}} \quad (2)$$

The repulsion term is expressed in the exponential Born–Mayer form, and it can be combined with the dispersive term, which is induced by interactions between the instantaneous dipole moments and their induced instantaneous dipole moments. The two short-range terms combined are known as the Buckingham potential, which was used in the current calculations. The two-body Buckingham potential is mathematically expressed as:

$$\varphi_{ij}^{\text{Buckingham}}(r_{ij}) = A \exp\left(-\frac{r_{ij}}{\rho}\right) - \frac{C_6}{r_{ij}^6}. \quad (3)$$

A , ρ , and C_6 are the Buckingham parameters. In practice, it is computationally impractical to include interactions between all atoms in the solid as the number of atoms are on a scale of 10^{23} and Buckingham interactions rapidly diminish with interatomic distance. To strike a balance between efficiency and accuracy, distance cut-offs are introduced. Typically, a value of 5–10 Å is used. A cut-off distance of 10 Å and 12 Å were set for cation–oxygen and oxygen–oxygen potentials, respectively, in this work. The Ewald Summation method was employed in the calculations of electrostatic interactions due to the slow convergence of $1/r$ summations. The arrangement of ions in the system is then determined by energy minimization processes with respect to all relevant structure factors, i.e., unit cell parameters and atomic coordinates [38].

Atoms are treated as point ions, using the core–shell model proposed by Dick and Overhauser [40] to account for the polarizability of ions. The shell model mimics an ion’s polarizability by defining an ion as an entity consisting of a shell and a core that interact through a spring constant K_{CS} . If the charges distributed on the shell of the ion are Q_s , the polarisability of the free ion can be expressed as

$$\alpha = \frac{Q_s^2}{K_{\text{CS}}} \quad (4)$$

The sum of the core and shell charges is equal to the formal oxidation state of respective ions. If all charges are on the core, the atom is considered to be unpolarizable. In the current simulations, the cationic core is treated as a rigid ion, and the charge distributions of O^{2-} are 0.869 e and -2.869 e on the core and shell, respectively. The K_{CS} of O^{2-} is 74.9.

As for energy minimisation, a quadratic approximation (the second-order Taylor expansion) is applied to the calculation of lattice energy:

$$E_{\text{Lattice}}(x) = E(x_k) + \Delta x \frac{dE_{\text{Lattice}}(x_k)}{dx_k} + (\Delta x)^2 \frac{1}{2!} \frac{d^2E_{\text{Lattice}}(x_k)}{d^2x_k} + O((\Delta x)^2) \quad (5)$$

where x represents atomic coordinates. A modified Newton–Raphson method is used for energy minimization with a step search direction Δx expressed as

$$\Delta x = -\alpha H^{-1}g. \quad (6)$$

where α is the modified co-efficient determined via line search g is the gradient vector, and H^{-1} is the inverse of the second derivative matrix (Hessian matrix), whose calculation is

the most computationally expensive step. The Broyden–Fletcher–Goldfarb–Shannon (BFGS) hessian matrix updating scheme is used by default, as the built-in minimisation process.

The Mott–Littleton (ML) method is used for calculations of defect formation energies. Atoms in the regions with different distances to the assigned defect centre are treated differently. The ML method divides the whole system studied into three regions, specifically, Region 1, Region 2b, and Region 2a. Atoms in Region 1 are treated explicitly. Region 2b is treated as a continuous dielectric medium whose energy is evaluated using classical continuum theory and atomic displacements are determined via bulk polarization. Region 2a is treated both atomistically and as a dielectric continuum to provide consistency between Region 1 and Region 2b [38,41,42]. The radii of Region 1 and Region 2a were set to be 20 Å and 30 Å, respectively. Experience tells us that these are sufficiently large to allow complete structural relaxation around the defects to eliminate this as a source of uncertainty in the defect energies.

Calculations of lattice energy were performed as the first step for simulations. The lattice energy is the cohesive energy that keeps atoms in a crystal binding with each other. If the energy where all atoms are at an infinite distance from each other is defined as zero, then a negative value is assigned to lattice energy. The two-body Buckingham potential parameters used in the current simulations are listed in Table 2, which were derived by Lewis and Catlow [43]. Li–O potential parameters came from earlier work by Cormack, and the optimized crystal structure, calculated lattice energy, and bulk modulus of Li₂O using the potential agree well with other simulations and experimental results [44–46]. Initial structural information about the three oxide crystalline materials involved was derived from the literature [44–48]. The lattice energies of MgO, Nd₂O₃, and Li₂O after optimizations are shown in Table 3.

Table 2. Buckingham potential parameters used in calculations.

Pairwise Interaction	A (eV)	ρ (Å)	C_6 (eV·Å ⁶)
Mg–O	820.8	0.3242	0
O–O	22764	0.149	27.879
Li–O	235.1	0.35441	0
Nd–O	1379.9	0.3601	0

Table 3. Calculated lattice energies.

Crystalline Materials	Lattice Energy per Formula (eV)
MgO	−40.55
Nd ₂ O ₃	−129.01
Li ₂ O	−29.67

3. Results and Discussions

3.1. Intrinsic Point Defects in Pristine MgO

Pristine crystalline MgO possesses a typical rock-salt structure (NaCl type) with a space group of Fm $\bar{3}$ m (No. 225), as shown in Figure 1. Given the relative ionic radius difference between O^{2−} and Mg²⁺, respectively, 1.21 Å and 0.86 Å [49], the structure can be described as the cations occupying the octahedral coordination site within cubic close-packed anion arrays. Ideally, both Mg²⁺ and O^{2−} ions are sitting in a perfect octahedral coordination environment. Each octahedron is connected by edge-sharing and corner-sharing with other octahedra of the same ion species. The bond length after bulk optimisation was calculated to be 2.105 Å.

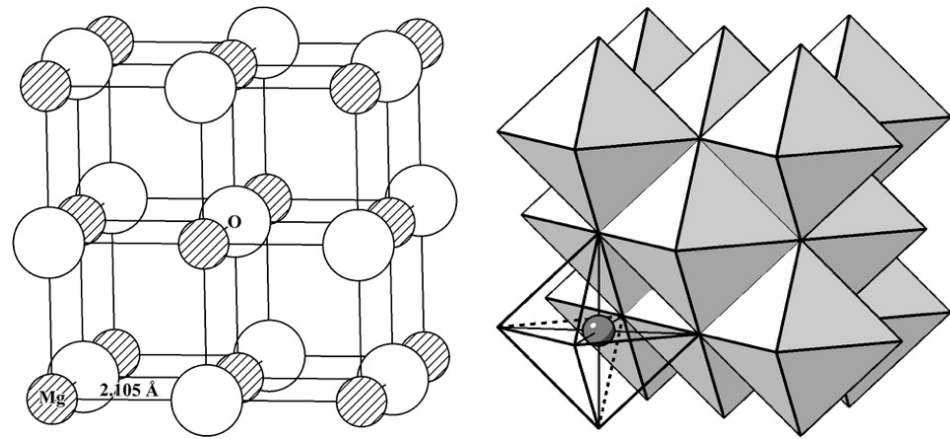
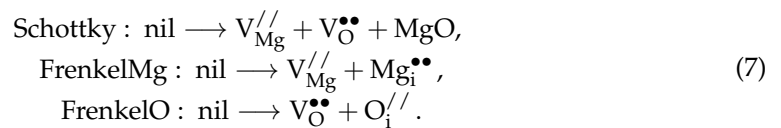


Figure 1. Rock-salt structure of MgO and ideal octahedral coordination.

For undoped MgO, the intrinsic defects considered include Schottky defect and Frenkel defects, in which four basic point defects are involved. Using Kröger–Vink notation, intrinsic point defects include Mg vacancy $V_{Mg}^{//}$, Mg interstitial $Mg_i^{••}$, O vacancy $V_O^{••}$, and O interstitial $O_i^{//}$. In the Kröger–Vink notations, V and i indicate vacancy and interstitial sites, respectively. The superscript forward slash (/) and dot (•) indicate a negative and positive effective charge possessed by the point defect, respectively. For example, $Mg_i^{••}$ means a Mg interstitial point defect with two positive effective charges. $Nd_{Mg}^{•}$ indicates a substitutional Nd (on Mg site) point defect with one positive effective charge. A superscript x means the defect has no effective charge. Schottky and Frenkel defects are expressed as



The calculated intrinsic defect formation energies per point defect are shown in Table 4. The current results are in reasonable agreement with experimental and other simulations [16,50–53]. The calculated lattice constant and Schottky energy are 4.210 Å and 6.22 eV, respectively, which agree well the experimental results of 4.207 Å [50] and 5–7 eV [53]. Here, Schottky and Frenkel defect energies are calculated using completely isolated point defects. Comparatively, the Schottky defect, which consists of one $V_{Mg}^{//}$ and one $V_O^{••}$, requires less formation energy. Thus, it is considered more favourable. A more favourable Schottky intrinsic defect indicates that when a vacancy is formed in pristine MgO another oppositely charged vacancy will be found with more probability for electrostatic compensation. As intrinsic vacancies are preferred, further speculation logically follows: substitution defects may be preferred in doped MgO. Within the cubic, close-packed anion array in the rock-salt structure, two types of interstitial sites are available: octahedral and tetrahedral. Classically, the ratio of ion size largely impacts which site is to be occupied. So, any dopant with a size slightly larger than Mg will be more likely to occupy the octahedral site and become a substitutional dopant on an Mg site. Fundamentally, which sites dopants will occupy depends on the characteristics of the introduced dopants, such as the effective charge or atomic size and the structure of the host material.

Table 4. Defect formation energies in pristine MgO.

Schottky energy (per point defect)	3.11 eV
Frenkel _{Mg} energy (per point defect)	5.18 eV
Frenkel _O energy (per point defect)	5.04 eV
$V_{Mg}^{//}$	22.96 eV

Table 4. Cont.

$V_{\text{O}}^{\bullet\bullet}$	23.81 eV
$Mg_{\text{i}}^{\bullet\bullet}$	−12.60 eV
$O_{\text{i}}^{\prime\prime}$	−13.75 eV

3.2. Point Defects and Defect Complexes in Neodymium Doped Magnesium

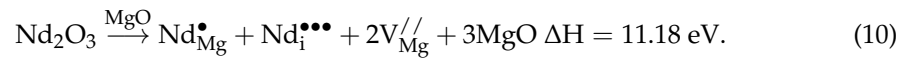
From the perspective of optical applications, the main purpose of doping active ions into a host material is, on the one hand, to take advantage of the unique physical properties of the host, such as thermal conductivity and intrinsic transparency; on the other hand, it is to take advantage of the crystal field of the host. The coordination environment (such as coordination number and coordination polyhedron) plays a significant role in doped optical materials as it had been observed and studied in crystal field theory [54]. When it comes to optical centres of rare earth ions, it is known that their electronic structures are less perturbed by the structure of the host material. The 4f orbitals are often unfilled, and they are well sheltered by the outer 5s5p orbitals according to the Aufbau principle. However, the optical properties of the doped system, or the absorption and emission of dopants are still impacted by the local atomic structure. The nature of doping means that the induced distortions in the host should not be ignored: that is, it is necessary to focus on the point defect configurations. In this section, point defects and defect complexes induced by Nd are investigated, and coordination distortions are revealed. By introducing Nd, two possible types of point defects are present, $Nd_{\text{i}}^{\bullet\bullet\bullet}$ and Nd_{Mg}^{\bullet} , and their defect formation energies were calculated to be −19.53 eV and −11.37 eV, respectively. These are the two forms in which Nd can be incorporated into MgO.

Two critical questions require consideration: From the point of energy, firstly, which is the more favourable way for Nd to be doped into MgO: $Nd_{\text{i}}^{\bullet\bullet\bullet}$ or Nd_{Mg}^{\bullet} ? Secondly, which is the more favoured defect that exists as the negative charge compensator for the Nd dopants: $V_{\text{Mg}}^{\prime\prime}$ or $O_{\text{i}}^{\prime\prime}$? To answer these questions, 22 quasi-chemical reactions were formulated under conservation and electroneutrality rules and are listed in Appendix A. The enthalpy per rare earth doping of the reaction is considered a benchmark for quantitative evaluations of the probability of obtaining certain defect configurations practically. For example, in reaction (8), $\Delta H(\text{perNd}) = \frac{1}{2} \times [(2 \times E_{\text{NdMg}}^{\text{f}} + E_{\text{VMg}}^{\text{f}} + 3 \times E_{\text{MgO}}^{\text{l}}) - E_{\text{Nd}_2\text{O}_3}^{\text{l}}]$, where E^{f} is the defect formation energy of point defect, E^{l} is the lattice energy of crystalline oxide. Point defects are isolated from each other at this point in the analysis. The defect reaction with the lowest enthalpy was found to involve three-point defects, two Nd substitutions on Mg sites, and one Mg vacancy as a charge compensator, and the enthalpy was calculated to be 3.79 eV per Nd doping. Another possible charge compensator for Nd_{Mg}^{\bullet} is $O_{\text{i}}^{\prime\prime}$:



The enthalpies shown are normalised to per Nd atom doping. The magnesium vacancy is the favoured compensator for positively charged defects instead of oxygen interstitial since its enthalpy is lower, as shown in reactions (8) and (9). On the other hand, in the rock-salt structure of MgO, the available tetrahedral interstitial sites are the sites surrounded by four oxygen anions. So, when oxygen is placed on one of these interstitial sites, immense relaxation of the lattice must then be induced because of the large electrostatic repulsions among local anions; this is undoubtedly less favoured for a negatively charged compensator to exist naturally.

The result also indicates that Nd favours substitution on the Mg site instead of an interstitial site in the MgO host. The reactions with the lowest enthalpy changes where one and two Nd_i are involved were found to be



It is quite straightforward to see that the magnitude of the effective charge becomes higher when Nd_i appears. The more Nd dopants that exist in the form of interstitials, the more magnesium vacancies are needed for charge compensation, which has a positive value of formation energy. It undoubtedly increases the enthalpy of the solution. Also, from the point of view of ionic size and effective charge, an Nd interstitial will result in more distortions to the host structure.

When point defects approach close to each other, the defect complexes can be formed. The defect complex must be considered to further determine the more favoured way to accommodate Nd dopants and the more favoured charge compensator. The mutual interactions between the point defects in a complex may influence the enthalpies of defect reactions. The way in which different configurations of defect complexes were tested involved using the Mg atom at the origin (0, 0, 0); either substitutional or interstitial point defects were placed on the available sites around it within a volume of 74.62 \AA^3 , which is the volume of one MgO unit cell. In the current context, the association energy is defined as the energy difference between the defect formation energy of a complex and the sum of the defect formation energies of those isolated point defects:

$$E_{\text{association}} = E_{\text{complex}} - \sum_{i=1}^n E_{\text{defect}}^i \quad (12)$$

E_{complex} is the defect energy of the defect complex, E_{defect}^i is the defect energy of an isolated point defect, and n is the total number of point defects in the defect complex. The clustering of point defects is called a complex normally when $n \geq 3$, but the formulation of $E_{\text{association}}$ for a pair of point defects is the same. A positive value of association energy is, as a result of this, considered unfavoured as it will increase the enthalpy when being taken into the quasi-chemical reaction. A negative value of association energy is considered to be favoured as it will decrease the enthalpy. It is determined mainly by the relative positions of point defects.

Defect pairs of two-point defects with oppositely effective charges, where Nd dopants are involved, were first considered. The lowest association energy (the highest absolute value) in each complex is listed in Table 5.

Table 5. Association energies of point defect pairs in Nd:MgO.

Defect Pair	Effective Charge (e)	Association Energy (eV)
$\text{Nd}_i^{\bullet\bullet\bullet} + V_{\text{Mg}}^{//}$	+1	−14.81 *
$\text{Nd}_i^{\bullet\bullet\bullet} + O_i^{//}$	+1	−4.12
$\text{Nd}_{\text{Mg}}^\bullet + V_{\text{Mg}}^{//}$	−1	−1.07
$\text{Nd}_{\text{Mg}}^\bullet + O_i^{//}$	−1	−1.63

* The relaxed configuration is the $\text{Nd}_{\text{Mg}}^\bullet$ point defect.

It was found in the simulations that when $\text{Nd}_i^{\bullet\bullet\bullet}$ was initially placed at $(\frac{1}{4}, \frac{1}{4}, \frac{1}{4})$, close to the (0, 0, 0) $V_{\text{Mg}}^{//}$, the Nd atom moved into the vacancy position after relaxation, with a formation energy the same as $\text{Nd}_{\text{Mg}}^\bullet$ (−11.37 eV). If Nd favours an interstitial site in MgO, the association energy of the $(\text{Nd}_i^{\bullet\bullet\bullet} + V_{\text{Mg}}^{//})$ pair is expected to be a positive value.

The calculated negative value of the association energy of $(\text{Nd}_i^{\bullet\bullet\bullet} + \text{V}_{\text{Mg}}^{//})$ shows that the favoured way to accommodate Nd in MgO is the substitution on the Mg site and not an interstitial site. Taking the association energies of the four defect pairs of Table 5 into the quasi-chemical reactions, one of the lowest enthalpies was found to be



It is the same set of reaction as shown in reaction (8). The information that can be extracted, so far, according to those results is: There are great probabilities that dopant Nd exists in the form of $\text{Nd}_{\text{Mg}}^{\bullet}$, and that $\text{V}_{\text{Mg}}^{//}$ is more favoured as a charge compensator rather than $\text{O}_i^{//}$.

To further investigate the structures of defects in Nd:MgO, the defect complex containing three individual point defects $(2\text{Nd}_{\text{Mg}}^{\bullet} + \text{V}_{\text{Mg}}^{//})_{\text{complex}}$ was considered. A total of 35 different configurations were tested to find the structure of the minimised formation energy. Initially, a magnesium vacancy was fixed at the origin, and configurations were tested by putting the other two Nd substitutions in other available Mg sites. It was found that associations between these three-point defects can further reduce the normalised reaction enthalpy to 2.72 eV, a reduction of 28% when all point defects are isolated as in reaction (8) and the relaxed structure of this defect complex is shown in Figure 2a.

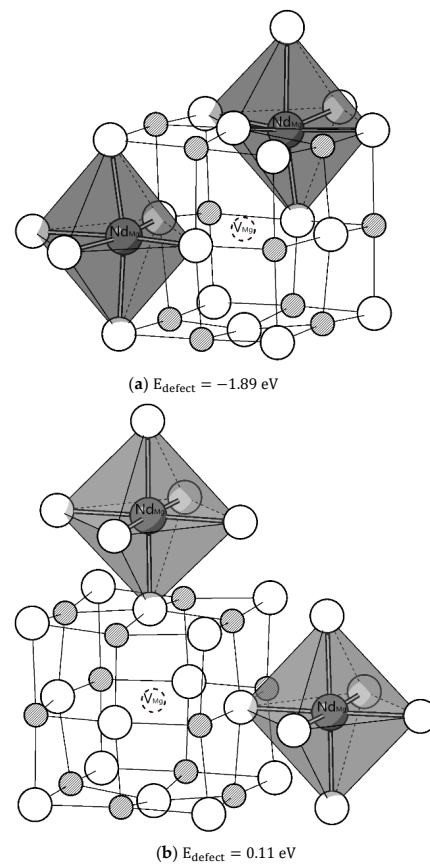
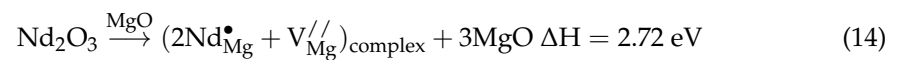


Figure 2. Defect structure of $(2\text{Nd}_{\text{Mg}}^{\bullet} + \text{V}_{\text{Mg}}^{//})_{\text{complex}}$: (a) the lowest E_{defect} configuration; (b) the highest E_{defect} configuration.

Figure 2a shows that both Nd substitutional defects remain in octahedral coordination with distortions to the polyhedron in bond angle and bond length. Figure 2b shows the

found configuration of the highest defect energy. The interatomic distances of Nd and the distances between point defects are listed in Table 6.

Table 6. Defect structure of $(2\text{Nd}_{\text{Mg}}^{\bullet} + \text{V}_{\text{Mg}}^{\prime\prime})_{\text{complex}}$.

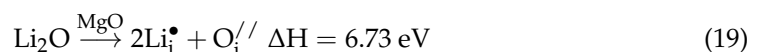
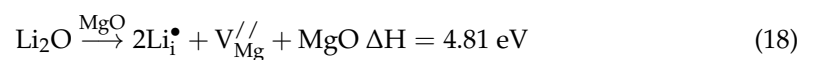
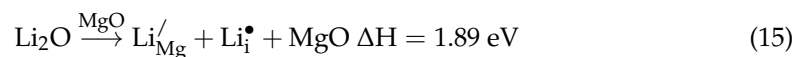
Distance	Configuration (a) (Å)	Configuration (b) (Å)
Average Nd–O	2.255	2.215
Average $\text{Nd}_{\text{Mg}}\text{--V}_{\text{Mg}}$	2.77	4.30
Nd–Nd	4.80	6.12

Compared to undoped MgO, where the optimised Mg–O length is 2.105 Å, the mean Nd–O lengths are around 2.255 Å and 2.215 Å for configurations (a) and (b), respectively. In configuration (a), changes in Mg–O bond length can be due to the changes in the electrostatic interaction between the substitutional defect and the surrounding oxygen ions. Although one Nd substitutional defect possesses a positive effective charge compared to the original Mg ion, thus polarizing the neighbouring oxide ions, which could result in a shorter bond length, Nd has a larger ionic size than Mg. When placed at the Mg site, the bond length increases after relaxation to accommodate it and this effect dominates. Two Nd dopants in configuration (a) are closer to the Mg vacancy compared to configuration (b), and they experience more powerful electrostatic interactions with Mg vacancy, exerting greater distortions on octahedral coordination. The interdopant distance Nd–Nd in configuration (a) is 4.80 Å, which is shorter than 6.12 Å in configuration (b). Comparisons of these two configurations show that it is energetically favourable for Nd dopants to aggregate in Nd:MgO.

Above all, it is more probable that Nd dopants exist as substitution defects on the Mg site with Mg vacancy as the charge compensator. A defect complex is more favoured than isolated point defects. In solely Nd-doped MgO, one may expect the existence of a Mg vacancy near substitutional Nd dopants.

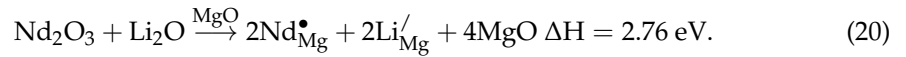
3.3. Influences of Lithium on Energetics and Defect Structures of Neodymium-Doped Magnesium Oxide

According to the experimental results obtained by Dorel [12], ionic exchange between Nd and Mg was not observed when MgO was the host. So, Nd dopants may not be successfully doped into the MgO host, or the quantity doped may have been too low to remain detectable. The difficulty of doping rare earth elements into MgO was also stressed by Sannamyan [13]. Li co-doping has been experimentally proven to improve the crystallinity and optical performance in rare-earth-doped MgO [6,9,10]. It is important to ask the following questions: In which way is Li making an impact? Does Li make it easier for Nd to enter the MgO host? The standing points to view the questions here are structure and energy. A similar procedure as in Nd:MgO was conducted: defect and association energies were calculated for Nd, Li:MgO. Via Li co-doping, two extra possible point defects are introduced— Li_i^{\bullet} and $\text{Li}_{\text{Mg}}^{\prime}$ —and the defect energies were calculated to be -1.23 eV and 15.89 eV, respectively. The quasi-chemical reactions for these two-point defects in Li:MgO are as follows:



The most favourable way to accommodate Li in MgO is $\text{Li}_{\text{Mg}}^{\prime}$ and Li_i^{\bullet} compensating for each other, as shown in reaction (15). By comparing reactions (16) and (18), $\text{Li}_{\text{Mg}}^{\prime}$ is relatively more favourable than Li_i^{\bullet} in MgO.

Applying the point defects of Nd and Li to the quasi-chemical reactions (56 possible reactions are shown in Appendix A), the one with the lowest enthalpy was found to contain two Nd substitutional and two Li substitutional point defects on Mg sites:



The defect complexes considered and their respective calculated association energies are listed in Table 7.

Table 7. Association energies of defect pairs in Nd, Li:MgO.

Defect	Effective Charge (e)	Association Energy (eV)
$(\text{Nd}_{\text{Mg}}^{\bullet} + \text{Li}_{\text{Mg}}^{\prime})_{\text{pair}}$	0	−0.53
$(2\text{Nd}_{\text{Mg}}^{\bullet} + \text{Li}_{\text{Mg}}^{\prime})_{\text{complex}}$	+1	−0.77
$(2\text{Li}_{\text{Mg}}^{\prime} + \text{Nd}_{\text{Mg}}^{\bullet})_{\text{complex}}$	−1	−0.84
$(2\text{Nd}_{\text{Mg}}^{\bullet} + 2\text{Li}_{\text{Mg}}^{\prime})_{\text{complex}}$	0	−1.60

Figure 3 shows the data points of simulation results regarding the relations between association energy and effective charge (EC) or the number of point defects (N) in defect complexes. Defect complexes containing more point defects with electroneutral effective charges are more favourable. The range of association energy is broadened by including more point defects in the complex. The ranges for a two-, three-, and four-point defect complex are 0.39 eV, 0.93 eV, and 1.60 eV. When more point defects join the complex, more configurations become possible, increasing the range. It shows that the range of association energy strongly depends on the relative atomic arrangements of included point defects. That is why it is necessary to conduct a systematic investigation to determine the most favourable defect structure. Depending on the specific atomic arrangement, associations can be favoured or unfavoured. This dependence on positions only occurs when the effective charge possessed by the defect complex is non-zero (−1 or +1 in the current case). The associations are always favoured when $EC = 0$, in both $N = 2$ and $N = 4$. With an increased N, it is more promising to find lower association energy. So far, the most potentially favourable defect complex in Nd, Li: MgO was found to be a $(2\text{Nd}_{\text{Mg}}^{\bullet} + 2\text{Li}_{\text{Mg}}^{\prime})_{\text{complex}}$ with zero effective charges. The relative positions of the point defects included do not change the sign of association energy, but the range of the association energy of four-point-defect complex is the largest compared to the complex with two- or three-point defects. The quasi-chemical reaction with the lowest enthalpy is



Remember that in Nd:MgO the Mg vacancy was found to be the favourable charge compensator for the Nd-substitution point defect. With Li co-doping, Li substitution point defects play the role of the charge compensator. Compared to the Mg vacancy with two negative effective charges and a vacant site within the crystalline lattice, the substitution by Li possesses one negative effective charge without leaving any charged vacant space, so $\text{Li}_{\text{Mg}}^{\prime}$ causes less structural perturbation to the crystal structure of MgO compared to $\text{V}_{\text{Mg}}^{\prime\prime}$. This result shines light on why Li co-doped materials have better crystallinity.

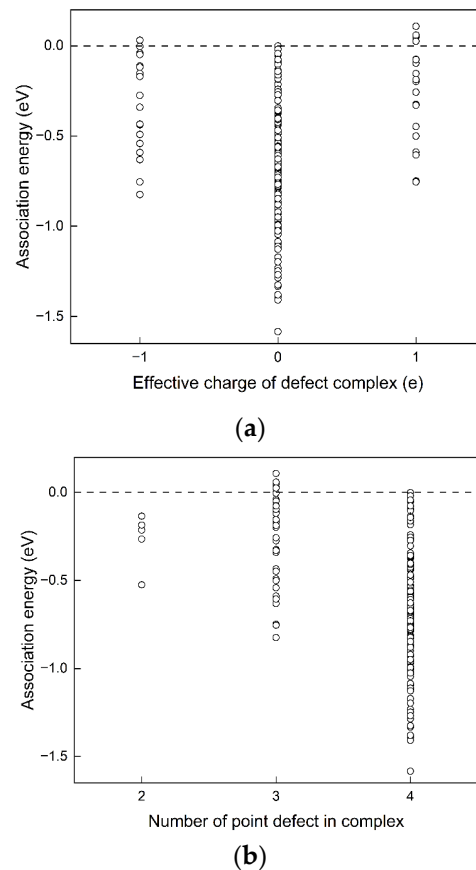


Figure 3. Association energies of defect complex containing $\text{Nd}_{\text{Mg}}^{\bullet}$ and $\text{Li}_{\text{Mg}}^{\prime}$: (a) $E_{\text{association}}$ vs. EC ; (b) $E_{\text{association}}$ vs. N .

Even though the MgO in the rock-salt structure is of high symmetry, point defects break the perfect local symmetry and result in many possible configurations. One Nd substitution defect was first fixed at the origin position (0, 0, 0). The number of possible configurations of the $(2\text{Nd}_{\text{Mg}}^{\bullet} + 2\text{Li}_{\text{Mg}}^{\prime})_{\text{complex}}$ was then C_{13}^3 , including some double counts. Thus, to put the other three cation substitutions on other available neighbouring Mg sites within the volume of one unit cell, 280 possible configurations were tested to find the favourable defect structure of $(2\text{Nd}_{\text{Mg}}^{\bullet} + 2\text{Li}_{\text{Mg}}^{\prime})_{\text{complex}}$.

The relaxed structure of the configuration with the lowest defect energy E_{defect} is shown in Figure 4a. Figure 4b shows the configuration that has the highest defect energy found. Interatomic distances of the two configurations are listed in Table 8.

The configuration with the lower defect energy is more disordered in bond length bond angle. Li favours a position close to Nd. Compared to the enthalpy of 2.72 eV obtained in reaction (14) without the co-dopant, in reaction (21), incorporating Li reduces the enthalpy by 28%. This result indicates that Nd can be doped into MgO more easily with Li as a co-dopant. Structurally, firstly, the Li has a smaller ion size than Mg, which is beneficial for the additional doping of large rare earth elements. Secondly, the relaxation of the O atom, which is surrounded by four substitutional point defects, causes large displacements in its position, as shown in Figure 5. Two Nd substitutional point defects are located at two sides of the oxygen atom, making it an equilibrium Coulombic attraction condition; this displacement of the O atom is mainly attributed to the two Li substitutional point defects, because of a repulsive electrostatic interaction. From the point of the doping objective, the displacement of oxygen atom makes more room for the accommodations of two Nd-substitution dopants.

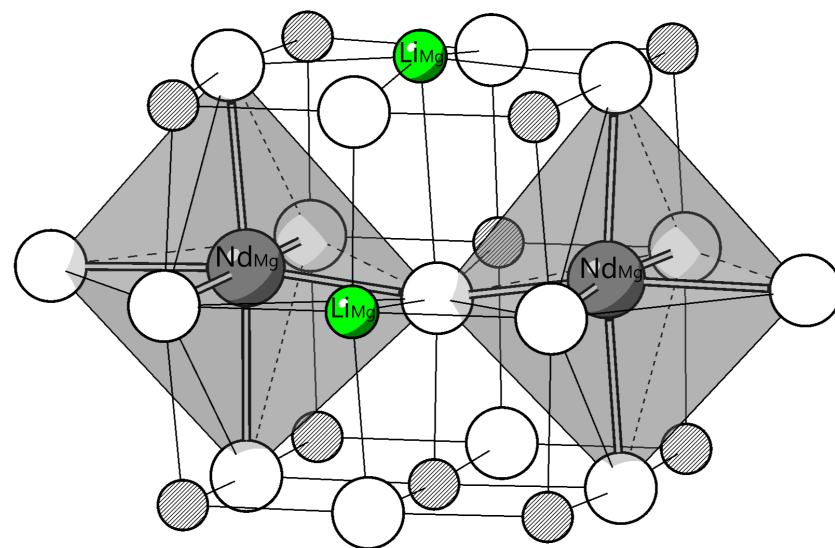
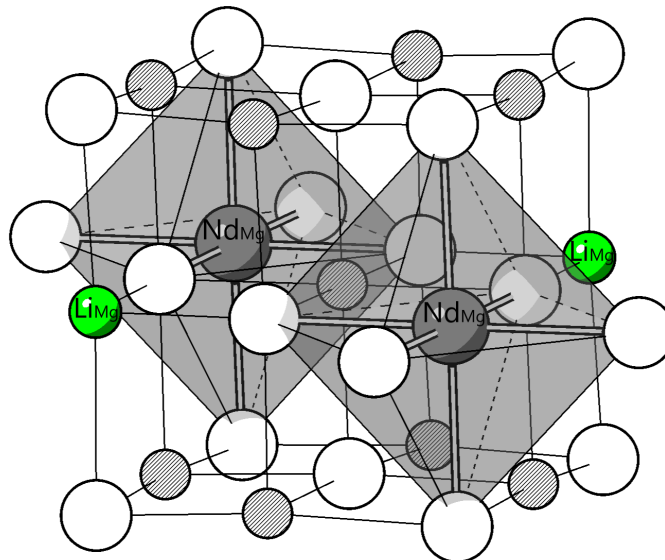
(a) $E_{\text{defect}} = 7.44 \text{ eV}$ (b) $E_{\text{defect}} = 8.97 \text{ eV}$

Figure 4. Relaxed structure of $(2\text{Nd}_{\text{Mg}}^{\bullet} + 2\text{Li}_{\text{Mg}}^{\bullet})_{\text{complex}}$: (a) the lowest E_{defect} configuration; (b) the highest E_{defect} configuration.

Table 8. Defect structure of $(2\text{Nd}_{\text{Mg}}^{\bullet} + 2\text{Li}_{\text{Mg}}^{\bullet})_{\text{complex}}$.

Interatomic Distance	The Lowest E_{defect} Configuration (Å)	The Highest E_{defect} Configuration (Å)
Average Nd-O	2.232	2.217
Average Nd-Li	3.154	4.230
Nd-Nd	4.130	6.093
Li-Li	3.384	5.868

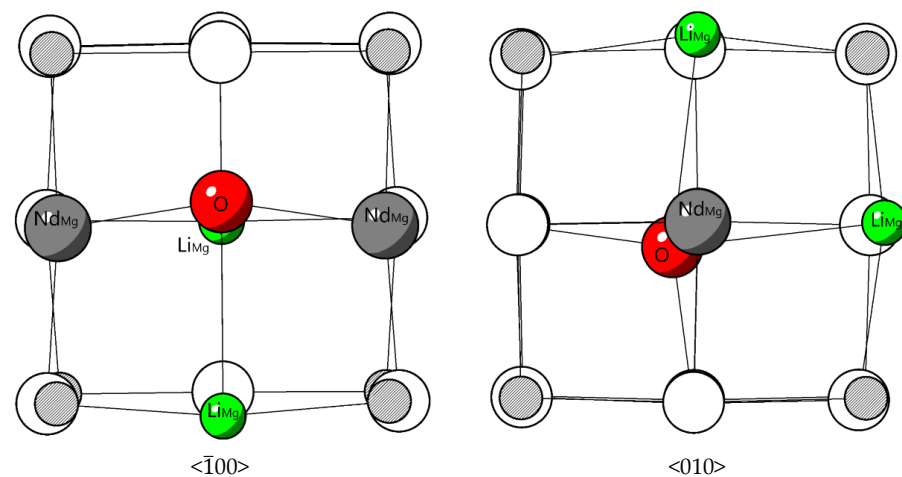


Figure 5. Relaxed structure of $(2\text{Nd}_{\text{Mg}}^{\bullet} + 2\text{Li}_{\text{Mg}}^{\wedge})_{\text{complex}}$ from $\langle \bar{1}00 \rangle$ and $\langle 010 \rangle$ directions.

The following question may be raised: What is the correlation between the defect energy of a defect complex and its configuration—the exact atomic arrangements? Remember that the association energy in the current context is defined as $E_{\text{association}} = E_{\text{complex}} - \sum_{i=1}^n E_{\text{defect}}^i$ from Equation (12) (a negative value of $E_{\text{association}}$ is favoured as it means the E_{complex} has a lower defect energy than $\sum_{i=1}^n E_{\text{defect}}^i$ and it will decrease the reaction enthalpy). One might assume that the closer those point defects approach each other, the greater the association (the higher absolute value of association energy), the lower the defect energy they will have. But, the relationship between the configuration of defect complex and defect formation energy is not that simple, even in the MgO host, which has a relatively simple crystal structure.

As shown in Figure 6, in a single MgO unit cell, the arrangement for four substitutional point defects to stay as distant from each other as possible is to put them on four diagonal corners of the cubic as in (a). Nevertheless, this configuration is more favoured than the condition where all substitutions are located on four face diagonal sites, as in (b). Start from (b), moving one Li closer to the other three substitutional point defects as shown in (c), the defect energy decreases. From selected examples, it is not clear which interatomic distance (Nd–O, Nd–Nd, or Nd–Li) in the defect complexes is more significant for their defect energies (or association energies). To further investigate the correlations, interatomic distances were extracted from relaxed structures of defect complexes. The interatomic distances considered include Nd–Nd, Li–Li, average Nd–Li, average Nd–O bond length, and average Li–O distance (the distance between Li and the first nearest six O atoms). The scattered data points of $E_{\text{association}}$ vs. interatomic distance are shown in Figure 7.

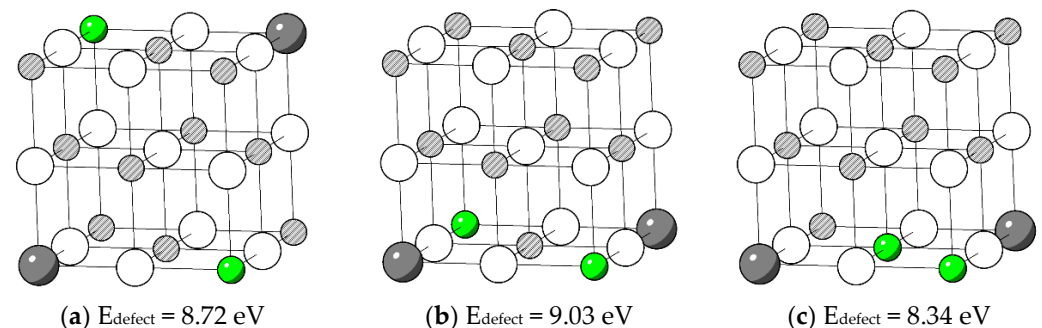


Figure 6. Selected test positions of $(2\text{Nd}_{\text{Mg}}^{\bullet} + 2\text{Li}_{\text{Mg}}^{\wedge})_{\text{complex}}$ and their defect energies. White: O. Green: Li. Grey: Nd. Striped: Mg.

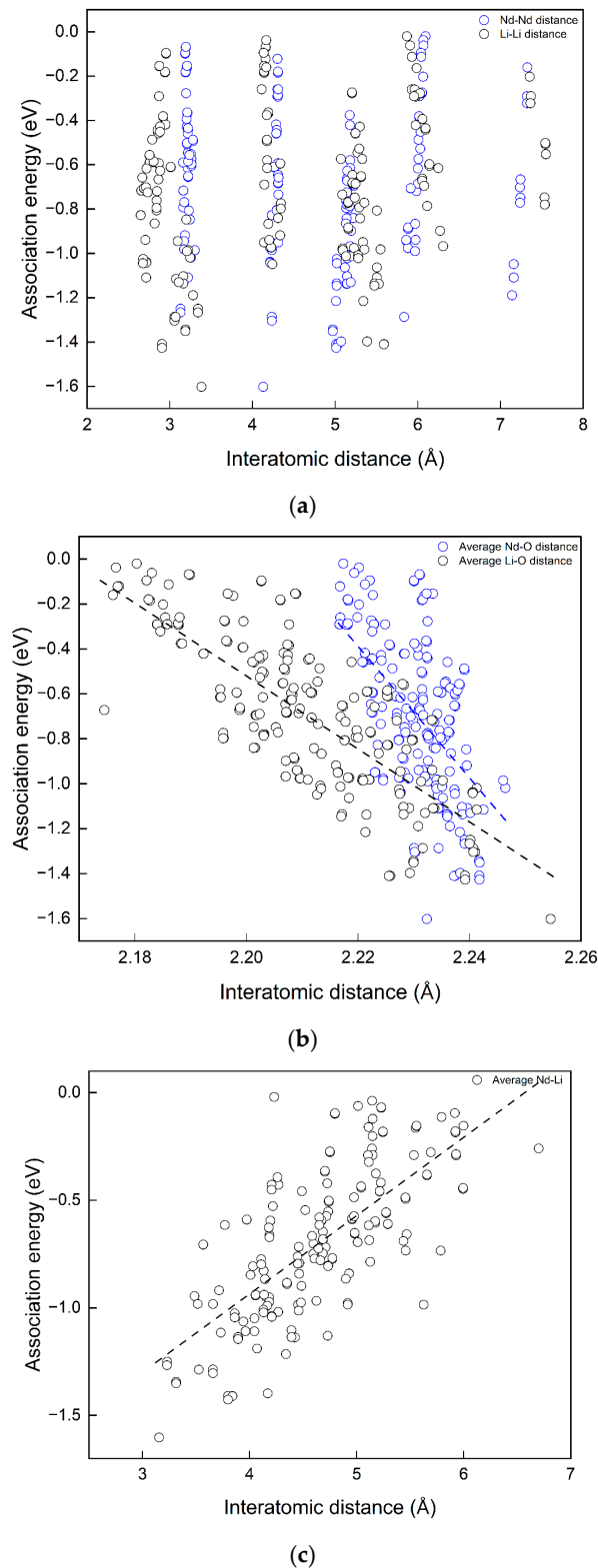


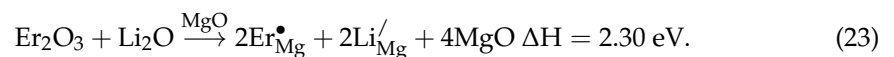
Figure 7. Correlations between interatomic distance and association energy: (a) Nd–Nd and Li–Li distance; (b) average Nd–O and Li–O distance; (c) average Nd–Li distance.

According to Figure 7a, there is no apparent dependency between $E_{\text{association}}$ and interatomic distances between two Nd dopants or two Li co-dopants in the complexes, since for each considered Nd–Nd and Li–Li distance high or low association energies are possible as in (a). On the contrary, dependencies of $E_{\text{association}}$ on Nd–Li, Nd–O, and Li–O

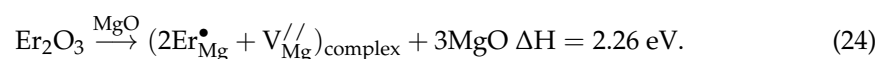
distances are clear in Figure 7b,c. The trend lines are shown as black dashed lines. Larger average Nd–O and Li–O are favoured for associations in the cluster. A shorter average Nd–Li distance is favoured. The trend line of the average Nd–O bond length has the steepest gradient. The correlations are not simply linear: no single interatomic distance solely determines the magnitude of the association energies of the defect complex. This is the great difficulty in analysing the defect complexes. However, the results above can be used to estimate or compare association energies among defect complexes in different configurations. In other words, one may approximate the more energetically favourable defect structure by comparing average Nd–O, Li–O, or Nd–Li distances.

3.4. Comparisons with Erbium-Doped Magnesium Oxide

According to Sanamyan [13], besides Nd: MgO, Li was also found to have a direct positive impact on the doping and optical properties of Er:MgO. Er, Li:MgO has a better visible transparency than Nd, Li:MgO. It is meaningful to compare the doping of Er and Nd into MgO from the point of energy. Intuitively, it might be easier to dope Er than Nd, as Er possesses a smaller ionic size. Calculations were performed to investigate Er doped MgO from a theoretical aspect. Because of the unavailability of Er–O Buckingham potential parameters with the same O–O potential parameters in the literature, Er–O Buckingham parameters were derived via relaxed fitting with GULP. The derivation methods of the potential parameters were outlined by Lewis and Gale [37,55,56]. The sum of least squares method was utilized to measure the fitting quality. By fitting to the experimental results [57–59], the derived Er–O Buckingham parameters are $A = 1381.518$ eV, $\rho = 0.349$ Å, and $C_6 = 0$ eV·Å⁶. The lattice energy of Er₂O₃ was calculated to be -134.97 eV, and the defect energy of Er_{Mg}[•] and Er_i^{•••} was calculated to be -14.817 eV and -23.244 eV, respectively. For Er:MgO and Er, Li:MgO, the following quasi-chemical reactions were found to possess the lowest enthalpy:



Furthermore, defects of the complexes of $(2\text{Er}_{\text{Mg}}^{\bullet} + V_{\text{Mg}}^{\prime\prime})_{\text{complex}}$ and $(2\text{Er}_{\text{Mg}}^{\bullet} + 2\text{Li}_{\text{Mg}}^{\prime})_{\text{complex}}$ were considered. A total of 35 configurations of $(2\text{Er}_{\text{Mg}}^{\bullet} + V_{\text{Mg}}^{\prime\prime})_{\text{complex}}$ —the same as $(2\text{Nd}_{\text{Mg}}^{\bullet} + V_{\text{Mg}}^{\prime\prime})_{\text{complex}}$ —were tested and they were found to have the same lowest-formation-energy configuration. As for $(2\text{Er}_{\text{Mg}}^{\bullet} + 2\text{Li}_{\text{Mg}}^{\prime})_{\text{complex}}$, 22 configurations were selected from the 280 configurations that were tested in the $(2\text{Nd}_{\text{Mg}}^{\bullet} + 2\text{Li}_{\text{Mg}}^{\prime})_{\text{complex}}$. The range of the association energies of the 280 tested configurations of $(2\text{Nd}_{\text{Mg}}^{\bullet} + 2\text{Li}_{\text{Mg}}^{\prime})_{\text{complex}}$ is from -1.6 to 0 eV, as shown in Figure 7. Based on an energy interval of 0.2 eV, in total, 22 configurations of $(2\text{Nd}_{\text{Mg}}^{\bullet} + 2\text{Li}_{\text{Mg}}^{\prime})_{\text{complex}}$ were selected, whose association energies fell within the eight ranges from -1.6 to 0 eV. It was found that $(2\text{Er}_{\text{Mg}}^{\bullet} + 2\text{Li}_{\text{Mg}}^{\prime})_{\text{complex}}$ has the same favourable configuration as $(2\text{Nd}_{\text{Mg}}^{\bullet} + 2\text{Li}_{\text{Mg}}^{\prime})_{\text{complex}}$. The quasi-chemical reactions for Er:MgO and Er, Li:MgO of the lowest enthalpies were



It shows that associations are also favoured in Er:MgO and Er, Li:MgO. And, Li co-doping also lowers (by 30%) the enthalpy for Er doping into MgO, a similar effect as in Nd:MgO. Compared to reaction (14) of Nd:MgO ($\Delta H = 2.72$ eV) and (21) of Nd, Li:MgO

($\Delta H = 1.96$ eV), doping Er into the MgO host requires less energy: 2.26 eV for Er: MgO and 1.59 eV for Er, Li:MgO.

With respect to the coordination octahedra of the rare earth dopants in MgO, Figure 8 shows the information of the dopant-oxygen bond lengths of two dopant-centred octahedra in each of the doped systems. The two dopants possess the same octahedron in their respective systems. The bond length of Mg–O in the pristine MgO 2.125 Å is indicated by the black dashed line. Comparing the systems with Li and without Li, it is apparent that in Li co-doped systems, the Nd–O and Er–O bond lengths—the maximum, the mean, and the minimum bond lengths—are shorter. Compared to Nd, Er has the shorter bond lengths. Besides the bond lengths, their distorted coordination octahedra also have distorted bond angles. A method to describe the distortions of a polyhedron systematically was proposed by Baur [60], where three distortion indices (DI) were defined: bond-length distortion, bond-angle distortion, and edge-length distortion (edge of the polyhedron). These distortion indices were originally defined for tetrahedral polyhedra. For octahedral polyhedron, analogous expressions of three distortion indices are [61]:

$$\begin{aligned} DI(\text{TO}) &= \left(\sum_{i=1}^6 |d_i - d_m| \right) / 6 \times d_m, \\ DI(\text{OTO}) &= \left(\sum_{i=1}^{12} |\alpha_i - \alpha_m| \right) / 12 \times \alpha_m, \\ DI(\text{OO}) &= \left(\sum_{i=1}^{12} |l_i - l_m| \right) / 12 \times l_m. \end{aligned} \quad (26)$$

where d stands for the bond length between the cation atom T and oxygen atom O, α stands for bond angle, l stands for edge length of octahedral polyhedron, and m indicates the mean value of each quantity. The calculated DI of the dopant-centred octahedra are listed in Table 9.

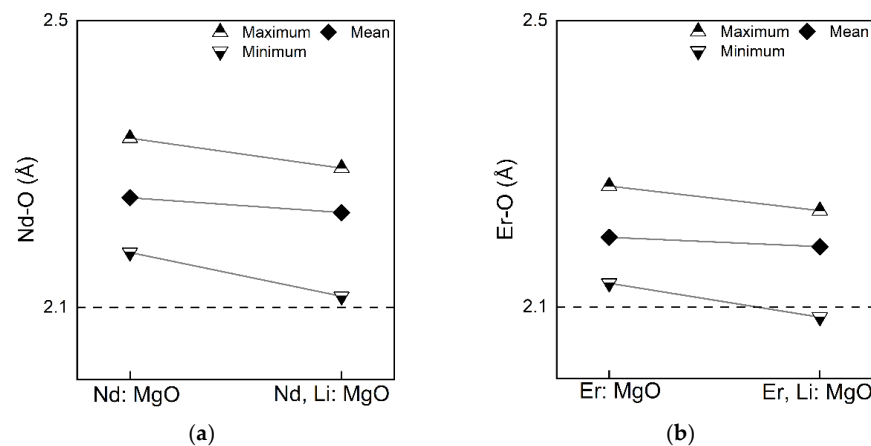


Figure 8. Comparisons of RE–O bond lengths in RE:MgO and RE, Li:MgO. RE = Nd or Er. Grey line: trend line: (a) Nd:MgO and Nd, Li:MgO; (b) Er:MgO and Er, Li:MgO.

With the Baur method, RE:MgO and RE, Li:MgO have similar DIs for bond-length and edge-length distortions. The DIs of bond-angle distortions in RE:MgO are relatively higher than in RE, Li:MgO. This is due to the high effective charges (-2) possessed by the Mg vacancy, causing large repulsions of the O atoms near the Mg vacancy. The difference between each quantity and the respective mean value is in an order of magnitude of -1 (0.1), so the calculated indices are in an order of magnitude of -2 (0.01). So, it is sufficient to keep the third significant figure of the numerical value when comparing degrees of distortions between octahedra. This information on the bond lengths and the distortions described above may be useful for comparative spectroscopic studies of active

RE ions in RE:MgO and RE, Li:MgO, where the local symmetries are decisive for the optical properties.

Table 9. Distortion indices of relaxed octahedra in the lowest energy configuration from static lattice calculations.

DI	Nd:MgO	Nd, Li:MgO
bond-length distortion	0.024	0.023
bond-angle distortion	0.064	0.051
edge-length distortion	0.032	0.032
DI	Er:MgO	Er, Li:MgO
bond-length distortion	0.021	0.021
bond-angle distortion	0.052	0.044
edge-length distortion	0.025	0.026

3.5. Incorporating Additional Li Co-Dopants

According to reaction (21), the defect complex discussed was $(2\text{Nd}_{\text{Mg}}^{\bullet} + 2\text{Li}_{\text{Mg}}^{\prime})_{\text{complex}}$ where the ratio between Nd and Li was 1:1. What will happen when more Li ions are introduced into the system? It is meaningful to consider the excess-Li condition? In the experimental practice, the mole ratio between doped Nd and Li is 1:3 [6]. Based on the results obtained in the last section (reactions (15) and (21), and the most favourable configuration of $(2\text{Nd}_{\text{Mg}}^{\bullet} + 2\text{Li}_{\text{Mg}}^{\prime})_{\text{complex}}$), the defect complex $(2\text{Nd}_{\text{Mg}}^{\bullet} + 2\text{Li}_{\text{Mg}}^{\prime} + 2\text{Li}_{\text{Mg}}^{\prime} + 2\text{Li}_{\text{i}}^{\bullet})_{\text{complex}}$ was considered. Extra $2\text{Li}_{\text{Mg}}^{\prime}$ and $2\text{Li}_{\text{i}}^{\bullet}$ were placed around the most favourable configuration of $(2\text{Nd}_{\text{Mg}}^{\bullet} + 2\text{Li}_{\text{Mg}}^{\prime})_{\text{complex}}$. In this defect complex, there are two Nd atoms and six Li atoms (Nd:Li = 1:3 or Nd, 3Li:MgO). The excess $\text{Li}_{\text{Mg}}^{\prime}$ point defects were placed at the nearest neighbouring Mg sites to Nd dopants, and the excess $\text{Li}_{\text{i}}^{\bullet}$ were tested for the eight nearest neighbouring interstitial sites to Nd dopants. The most favourable configuration of $(2\text{Nd}_{\text{Mg}}^{\bullet} + 4\text{Li}_{\text{Mg}}^{\prime} + 2\text{Li}_{\text{i}}^{\bullet})_{\text{complex}}$ that was found is shown in Figure 9 (ΔH is normalized to per Nd dopant). The bond length and inter-atomic distances are listed in Table 10. Note that the average Nd–O bond length is 0.01 Å shorter than that of Nd, Li:MgO. The interdopant distance is 0.17 Å longer than that of Nd, Li:MgO. The quasi-chemical reaction after excess-Li co-doping is shown in (27).

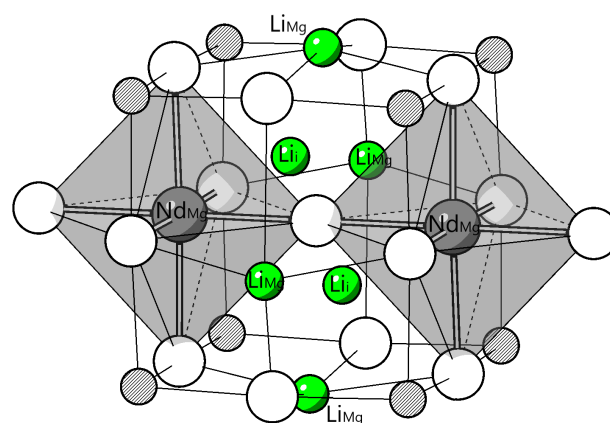
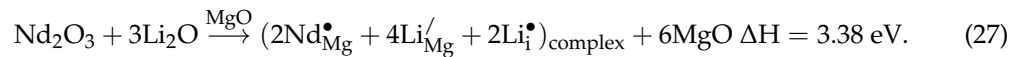


Figure 9. The most favourable configuration of $(2\text{Nd}_{\text{Mg}}^{\bullet} + 4\text{Li}_{\text{Mg}}^{\prime} + 2\text{Li}_{\text{i}}^{\bullet})_{\text{complex}}$.

Table 10. Defect structure of $(2\text{Nd}_{\text{Mg}}^{\bullet} + 4\text{Li}_{\text{Mg}}^{\prime} + 2\text{Li}_{\text{i}}^{\bullet})_{\text{complex}}$.

Interatomic Distance	(Å)
Average Nd–O	2.223
Average Nd–Li	3.160
Nd–Nd	4.301
Average Li–Li	3.475



Compared to reaction (21), co-doping excess Li into the MgO host requires extra energy of 1.42 eV per Nd dopant. Though the excess $2\text{Li}_{\text{Mg}}^{\prime}$ and $2\text{Li}_{\text{i}}^{\bullet}$ point defects are not needed for the charge compensation of the Nd dopants, they were found to have an impact on the distortion of the octahedral coordination geometry of Nd dopants. The calculated Baur DIs are shown in Table 11.

Table 11. Distortion indices of relaxed octahedra of Nd in excess-Li condition (Nd:Li = 1:3).

DI	Nd, 3Li:MgO
bond-length distortion	0.011
bond-angle distortion	0.012
edge-length distortion	0.006

Three distortion indices of octahedral coordination geometries of Nd dopants were found to decrease significantly in the excess-Li co-doped condition compared to Table 9. The reductions in the bond-length, bond-angle, and edge-length distortions are 52.2%, 76.5%, and 81.3%, respectively. The dramatic reductions of the distortion indices may be partially responsible for the experimentally observed increase in optical emission intensity via Li co-doping [6], considering that a less-distorted coordination geometry for Nd might contribute to more localized Stark levels in the 4f manifolds, which is beneficial to obtain emissions with less bandwidth and increased intensity [54,62].

4. Conclusions

The most energetically favourable structures of defect complexes in rare earth (Nd and Er)-doped MgO with and without Li co-doping were found using calculations of formation energies of point defects and their defect complexes. Both rare earth dopants Nd, Er, and Li co-dopants that prefer substitution on Mg sites. $\text{Li}_{\text{Mg}}^{\prime}$ provides charge compensation for the rare earth substitutional point defects and causes the relaxation of neighbouring O atoms, which helps to accommodate the rare earth dopants.

$\text{Li}_{\text{Mg}}^{\prime}$ replacing the Mg vacancy as a charge compensator may play an essential role in improving the crystallinity in co-doped materials compared to solely doped materials. Li co-doping reduces the energy required to dope Nd and Er into the MgO host. In polycrystalline samples, for example, since Li encourages the doping of rare earths into the host, the aggregations of dopants along the grain boundaries can be reduced. This contribution from Li would be practically meaningful for modifying concentration quenching and transparency, which are all closely related to the chemistry of grain boundaries. In other words, our results regarding the influence of Li on energetics indicate that greater amount of rare earth elements could be effectively doped into the MgO host through co-doping Li, in contrast to systems without Li. This can partially explain the experimental results [6,9,10] where the characteristic optical emission intensity of rare earth dopants is enhanced by co-doping Li in ceramic samples. Additionally, our calculations show that Er requires less energy than Nd to enter the MgO host. This suggests the possibility that there are

more aggregations of Nd than Er in the grain boundary, causing passive impacts on the transparency of ceramic samples. The result may explain the experimental finding [13] that Er-doped MgO exhibits superior visible transparency compared to Nd-doped MgO ceramic samples.

The correlations between the association energy and defect structure in the defect complex $(2\text{Nd}_{\text{Mg}}^{\bullet} + 2\text{Li}_{\text{Mg}}^{\prime})$ was investigated. The average distances between cations and the nearest oxygens and between Nd dopants and Li co-dopants were found to have a correlation with association energy. Besides interatomic distance, the breakdown of symmetry, local dipole moments, and interactions between the dipole moments may all have their roles in associations. Further studies on these physical quantities will provide a deeper understanding about the association between point defects in the defect complexes. Reduced distortions in the coordination octahedra of Nd and Er were found in systems co-doped with Li (in the form of $\text{Li}_{\text{Mg}}^{\prime}$). This result provides a potential explanation for the experimental findings [6,10,11] demonstrating improved crystallinity and optical emission intensity in rare-earth-doped MgO through Li co-doping. An excess-Li co-doping condition was also considered. It was found that increasing the ratio between Nd and Li from 1:1 to 1:3 led to a significant reduction in the calculated Baur Distortion Indices. The determination of the most favourable defect structure in rare-earth-doped MgO will contribute to further investigations into its electronic structures, thereby enhancing the understanding of the mechanism by which Li influences the optical properties of rare-earth-doped MgO.

Author Contributions: Conceptualization, A.N.C. and Y.W.; Investigation, Y.Z., A.N.C. and Y.W.; Methodology, A.N.C.; Supervision, A.N.C. and Y.W.; Writing—original draft, Y.Z.; Writing—review and editing, A.N.C. and Y.W. All authors have read and agreed to the published version of the manuscript.

Funding: This research received no external funding.

Data Availability Statement: The original contributions presented in the study are included in the article, further inquiries can be directed to the corresponding author.

Acknowledgments: The topic and methodology of this work were developed by Yiquan Wu and Alastair N. Cormack. The theoretical calculations were performed using computing resources at the Inamori School of Engineering at NYS College of Ceramics, Alfred University. YFZ would like to thank Doris Möncke and Alexis G. Clare for fruitful dialogues and thank Alfred University for studentships.

Conflicts of Interest: The authors declare no conflicts of interest.

Appendix A

Quasi-chemical defect reactions in Nd:MgO and Nd, Li:MgO.

Quasi-Chemical Reactions	ΔH per Nd Dopant (eV)
$\text{Nd}_2\text{O}_3 \xrightarrow{\text{MgO}} 2\text{Nd}_i^{\bullet\bullet\bullet} + \text{V}_O^{\bullet\bullet} + 4\text{O}_i^{\prime\prime}$	29.38
$\text{Nd}_2\text{O}_3 \xrightarrow{\text{MgO}} 2\text{Nd}_i^{\bullet\bullet\bullet} + \text{V}_O^{\bullet\bullet} + \text{V}_{\text{Mg}}^{\prime\prime} + 3\text{O}_i^{\prime\prime} + \text{MgO}$	27.46
$\text{Nd}_2\text{O}_3 \xrightarrow{\text{MgO}} 2\text{Nd}_i^{\bullet\bullet\bullet} + 3\text{O}_i^{\prime\prime}$	24.35
$\text{Nd}_2\text{O}_3 \xrightarrow{\text{MgO}} 2\text{Nd}_i^{\bullet\bullet\bullet} + \text{V}_O^{\bullet\bullet} + 3\text{V}_{\text{Mg}}^{\prime\prime} + \text{O}_i^{\prime\prime} + 3\text{MgO}$	23.62
$\text{Nd}_2\text{O}_3 \xrightarrow{\text{MgO}} 2\text{Nd}_i^{\bullet\bullet\bullet} + \text{V}_{\text{Mg}}^{\prime\prime} + 2\text{O}_i^{\prime\prime} + \text{MgO}$	22.43
$\text{Nd}_2\text{O}_3 \xrightarrow{\text{MgO}} 2\text{Nd}_i^{\bullet\bullet\bullet} + \text{V}_O^{\bullet\bullet} + 4\text{V}_{\text{Mg}}^{\prime\prime} + 4\text{MgO}$	21.69
$\text{Nd}_2\text{O}_3 \xrightarrow{\text{MgO}} 2\text{Nd}_i^{\bullet\bullet\bullet} + 2\text{V}_{\text{Mg}}^{\prime\prime} + \text{O}_i^{\prime\prime} + 2\text{MgO}$	20.51

Table A0. Cont.

Quasi-Chemical Reactions	ΔH per Nd Dopant (eV)
$2\text{Nd}_2\text{O}_3 + \text{Li}_2\text{O} \xrightarrow{\text{MgO}} 4\text{Nd}_{\text{Mg}}^{\bullet} + \text{O}_i^{\prime\prime} + 2\text{Li}_{\text{Mg}}^{\prime} + 6\text{MgO}$	4.24
$3\text{Nd}_2\text{O}_3 + \text{Li}_2\text{O} \xrightarrow{\text{MgO}} 6\text{Nd}_{\text{Mg}}^{\bullet} + \text{V}_{\text{Mg}}^{\prime\prime} + \text{O}_i^{\prime\prime} + 2\text{Li}_{\text{Mg}}^{\prime} + 9\text{MgO}$	4.09
$2\text{Nd}_2\text{O}_3 + \text{Li}_2\text{O} \xrightarrow{\text{MgO}} 4\text{Nd}_{\text{Mg}}^{\bullet} + \text{V}_{\text{Mg}}^{\prime\prime} + 2\text{Li}_{\text{Mg}}^{\prime} + 7\text{MgO}$	3.28
$\text{Nd}_2\text{O}_3 + \text{Li}_2\text{O} \xrightarrow{\text{MgO}} 2\text{Nd}_{\text{Mg}}^{\bullet} + 2\text{Li}_{\text{Mg}}^{\prime} + 4\text{MgO}$	2.76

References

- Kato, T.; Yanagida, T. Optical, Scintillation and Dosimeter Properties of MgO Translucent Ceramic Doped with Cr^{3+} . *Opt. Mater.* **2016**, *54*, 134–138. [[CrossRef](#)]
- Kato, T.; Okada, G.; Yanagida, T. Optical, scintillation and dosimeter properties of MgO transparent ceramic doped with Mn^{2+} . *J. Ceram. Soc. Jpn.* **2016**, *124*, 559–563. [[CrossRef](#)]
- Kato, T.; Okada, G.; Kawaguchi, N.; Yanagida, T. Dosimeter properties of Ce-doped MgO transparent ceramics. *J. Lumin.* **2017**, *192*, 316–320. [[CrossRef](#)]
- Kumamoto, N.; Kato, T.; Kawano, N.; Okada, G.; Kawaguchi, N.; Yanagida, T. Scintillation and dosimeter properties of Ca-doped MgO transparent ceramics. *Nucl. Instrum. Methods Phys. Res. B* **2018**, *435*, 313–317. [[CrossRef](#)]
- Fan, T.Y.; Cordova-Plaza, A.; Digonnet, M.J.F.; Byer, R.L.; Shaw, H.J. Nd: MgO: LiNbO₃ spectroscopy and laser devices. *J. Opt. Soc. Am. B* **1986**, *3*, 140–148. [[CrossRef](#)]
- Oliveira, L.; Milliken, E.; Yukihara, E. Development and characterization of MgO: Nd, Li synthesized by solution combustion synthesis for 2D optically stimulated luminescence dosimetry. *J. Lumin.* **2013**, *133*, 211–216. [[CrossRef](#)]
- Bindhu, M.; Umadevi, M.; Micheal, M.K.; Arasu, M.V.; Al-Dhabi, N.A. Structural, morphological and optical properties of MgO nanoparticles for antibacterial applications. *Mater. Lett.* **2016**, *166*, 19–22. [[CrossRef](#)]
- Blair, V.L.; Fleischman, Z.D.; Merkle, L.D.; Ku, N.; Moorehead, C.A. Co-precipitation of rare-earth-doped Y₂O₃ and MgO nanocomposites for mid-infrared solid-state lasers. *Appl. Opt.* **2017**, *56*, B154–B158. [[CrossRef](#)]
- Orante-Barrón, V.; Oliveira, L.; Kelly, J.; Milliken, E.; Denis, G.; Jacobssohn, L.; Puckette, J.; Yukihara, E. Luminescence properties of MgO produced by solution combustion synthesis and doped with lanthanides and Li. *J. Lumin.* **2011**, *131*, 1058–1065. [[CrossRef](#)]
- Gu, F.; Li, C.Z.; Jiang, H.B. Combustion synthesis and photoluminescence of MgO: Eu³⁺ nanocrystals with Li⁺ addition. *J. Cryst. Growth* **2006**, *289*, 400–404. [[CrossRef](#)]
- Sivasankari, J.; Sellaiyan, S.S.; Sankar, S.; Devi, L.V.; Sivaji, K. Structural and optical characterization of Er-alkali-metals co-doped MgO nanoparticles synthesized by solution combustion route. *Phys. E Low Dimens. Syst. Nanostruct.* **2017**, *85*, 152–159. [[CrossRef](#)]
- Crişan, D.; Drăgan, N.; Crişan, M.; Ianculescu, A.; Todan, L.; Védrine, J.C.; Filkova, D.; Gabrovská, M.; Kardjieva, R.E. Structural study of the MO-Nd₂O₃ system obtained by a sol-gel procedure. *Comptes Rendus Chim.* **2018**, *21*, 232–246. [[CrossRef](#)]
- Sanamyan, T.; Cooper, C.; Gilde, G.; Sutorik, A.C.; Dubinskii, M. Fabrication and spectroscopic properties of transparent Nd³⁺: MgO and Er³⁺: MgO ceramics. *Laser Phys. Lett.* **2014**, *11*, 065801. [[CrossRef](#)]
- Karki, B.B.; Khanduja, G. Vacancy defects in MgO at high pressure. *Am. Mineral.* **2006**, *91*, 511–516. [[CrossRef](#)]
- Gao, F.; Hu, J.; Yang, C.; Zheng, Y.; Qin, H.; Sun, L.; Kong, X.; Jiang, M. First-principles study of magnetism driven by intrinsic defects in MgO. *Solid State Commun.* **2009**, *149*, 855–858. [[CrossRef](#)]
- De Vita, A.; Gillan, M.J.; Lin, J.S.; Payne, M.C.; Štich, I.; Clarke, L.J. Defect energetics in MgO treated by first-principles methods. *Phys. Rev. B* **1992**, *46*, 964–973. [[CrossRef](#)] [[PubMed](#)]
- Gilbert, C.A.; Kenny, S.D.; Smith, R.; Sanville, E. Ab initio study of point defects in magnesium oxide. *Phys. Rev. B* **2007**, *76*, 184103. [[CrossRef](#)]
- Gibson, A.; Haydock, R.; LaFemina, J.P. Stability of vacancy defects in MgO: The role of charge neutrality. *Phys. Rev. B* **1994**, *50*, 2582–2592. [[CrossRef](#)]
- Ertekin, E.; Wagner, L.K.; Grossman, J.C. Monte Carlo methods: Application to the F-center defect in MgO. *Phys. Rev. B* **2013**, *87*, 155210. [[CrossRef](#)]
- Harding, J.H.; Sangster, M.J.L.; Stoneham, A.M. Cation diffusion in alkaline-earth oxides. *J. Phys. C Solid State Phys.* **1987**, *20*, 5281–5292. [[CrossRef](#)]
- Shluger, A.L.; Heifets, E.N.; Gale, J.D.; Catlow, C.R. Theoretical simulation of localized holes in MgO. *J. Phys. Condens. Matter* **1992**, *4*, 5711–5722. [[CrossRef](#)]
- Foot, J.; Colbourn, E.; Catlow, C. Computer simulation of alkali metal trapped hole defects in alkaline earth oxides. *J. Phys. Chem. Solids* **1988**, *49*, 1225–1232. [[CrossRef](#)]
- Kantorovich, L.N.; Kotomin, E.A. Quantum-chemical simulation of impurity-induced trapping of a hole: [Li]^o centre in MgO. *J. Phys. C Solid State Phys.* **1986**, *19*, 4183–4199.
- Pandey, R.; Kunz, A.B. Characterization of fluorine-doped magnesium oxide: A computer simulation study. *J. Phys. Chem. Solids* **1990**, *51*, 929–931. [[CrossRef](#)]

25. Pandey, R.; Zuo, J.; Kunz, A.B. Excitonic states in pure and impurity-doped magnesium oxide. *Phys. Rev. B* **1989**, *39*, 12565–12567. [[CrossRef](#)] [[PubMed](#)]
26. Zhang, D.; Lin, Y.; Song, S.; Zhang, P.; Mi, H. Study of the microstructure and antibacterial properties of MgO with doped defects. *J. Theor. Comput. Chem.* **2018**, *17*, 1850018. [[CrossRef](#)]
27. Yokoi, T.; Yoshiya, M. Atomistic simulations of grain boundary transformation under high pressures in MgO. *Phys. B Condens. Matter* **2017**, *532*, 2–8. [[CrossRef](#)]
28. Verma, A.K.; Karki, B.B. First-principles simulations of MgO tilt grain boundary: Structure and vacancy formation at high pressure. *Am. Mineral.* **2010**, *95*, 1035–1041. [[CrossRef](#)]
29. Watson, G.W.; Kelsey, E.T.; De Leeuw, N.H.; Harris, D.J.; Parker, S.C. Atomistic simulation of dislocations, surfaces and interfaces in MgO. *J. Chem. Soc. Faraday Trans.* **1996**, *92*, 433–438. [[CrossRef](#)]
30. de Leeuw, N.H.; Parker, S.C. Molecular-dynamics simulation of MgO surfaces in liquid water using a shell-model potential for water. *Phys. Rev. B* **1998**, *58*, 13901. [[CrossRef](#)]
31. Aidhy, D.S.; Millett, P.C.; Wolf, D.; Phillpot, S.R.; Huang, H. Kinetically driven point-defect clustering in irradiated MgO by molecular-dynamics simulation. *Scr. Mater.* **2009**, *60*, 691–694. [[CrossRef](#)]
32. Uberuaga, B.P.; Smith, R.; Cleave, A.R.; Henkelman, G.; Grimes, R.W.; Voter, A.F.; Sickafus, K.E. Dynamical simulations of radiation damage and defect mobility in MgO. *Phys. Rev. B Condens. Matter Mater. Phys.* **2005**, *71*, 104102. [[CrossRef](#)]
33. Alfè, D. The melting curve of MgO from first principles simulations. *Phys. Rev. Lett.* **2005**, *94*, 235701. [[CrossRef](#)] [[PubMed](#)]
34. Belonoshko, A.B.; Dubrovinsky, L.S. Molecular dynamics of NaCl (B1 and B2) and MgO (B1) melting: Two-Phase simulation. *Am. Mineral.* **1996**, *81*, 303–316. [[CrossRef](#)]
35. Strachan, W.A.G., III. Phase diagram of MgO from density-functional theory and molecular-dynamics simulations. *Phys. Rev. B* **1999**, *60*, 15084. [[CrossRef](#)]
36. Petersen, B.; Liu, B.; Weber, W.; Zhang, Y. Ab initio molecular dynamics simulations of low energy recoil events in MgO. *J. Nucl. Mater.* **2017**, *486*, 122–128. [[CrossRef](#)]
37. Gale, J.D.; Rohlf, A.L. The General Utility Lattice Program (GULP). *Mol. Simul.* **2003**, *29*, 291–341. [[CrossRef](#)]
38. Catlow, C.R.A.; Bell, R.G.; Gale, J.D. Computer modelling as a technique in materials chemistry. *J. Mater. Chem.* **1994**, *4*, 781. [[CrossRef](#)]
39. Dove, M.T. *Introduction to Lattice Dynamics*; Cambridge University Press: Cambridge, UK, 1993.
40. Dick, B.G.; Overhauser, A.W. Theory of the Dielectric Constants of Alkali Halide Crystals. *Phys. Rev.* **1958**, *112*, 90–103. [[CrossRef](#)]
41. Du, J.; Cormack, A.N. (Eds.) *Atomistic Simulations of Glasses*; Wiley: Hoboken, NJ, USA, 2022.
42. Tilley, R.J.D. *Defects in Solids*; John Wiley & Sons: Hoboken, NJ, USA, 2008.
43. Lewis, G.V.; Catlow, C.R.A. Potential models for ionic oxides. *J. Phys. C Solid State Phys.* **1985**, *18*, 1149. [[CrossRef](#)]
44. Goel, P.; Choudhury, N.; Chaplot, S.L. Superionic behavior of lithium oxide Li₂O: A lattice dynamics and molecular dynamics study. *Phys. Rev. B Condens. Matter Mater. Phys.* **2004**, *70*, 174307. [[CrossRef](#)]
45. Samsonov, G.V. *The Oxide Handbook*; Plenum: New York, NY, USA, 1982.
46. Hull, S.; Farley, T.; Hayes, W.; Hutchings, M. The elastic properties of lithium oxide and their variation with temperature. *J. Nucl. Mater.* **1988**, *160*, 125–134. [[CrossRef](#)]
47. Cimino, A.; Porta, P.; Valigi, M. Dependence of the Lattice Parameter of Magnesium Oxide on Crystallite Size. *J. Am. Ceram. Soc.* **1966**, *49*, 152–156. [[CrossRef](#)]
48. Kamwaya, M.E.; Oster, O.; Bradaczek, H. X-ray structure analysis and molecular conformation of tert-butyloxycarbonyl-L-prolylproline (Boo-Pro-Pro). *Acta Cryst.* **1981**, *37*, 1564–1568, Erratum in *Acta Cryst.* **1982**, *38*, 344. [[CrossRef](#)]
49. Shannon, R.D.; Prewitt, C.T. Effective Ionic Radii in Oxides and Fluorides. *Acta Cryst. B* **1969**, *25*, 925. [[CrossRef](#)]
50. Paier, J.; Marsman, M.; Hummer, K.; Kresse, G.; Gerber, I.C.; Ángyán, J.G. Screened hybrid density functionals applied to solids. *J. Chem. Phys.* **2006**, *125*, 154709. [[CrossRef](#)] [[PubMed](#)]
51. Sangster, M.J.L.; Rowell, D.K. Calculation of defect energies and volumes in some oxides. *Philos. Mag. A* **1981**, *44*, 613–624. [[CrossRef](#)]
52. Mackrodt, W.C.; Stewart, R.F. Defect properties of ionic solids. II. Point defect energies based on modified electron-gas potentials. *J. Phys. C Solid State Phys.* **1979**, *12*, 431. [[CrossRef](#)]
53. Mackrodt, W.C. Defect calculations for ionic materials. In *Computer Simulation of Solids*; Catlow, C.R.A., Mackrodt, W.C., Eds.; Springer: Berlin/Heidelberg, Germany, 1982; pp. 173–194.
54. Ikesue, A.; Aung, Y.L.; Lupei, V. *Ceramic Lasers*; Cambridge University Press: New York, NY, USA, 2013.
55. Lewis, G.V. Potentials: Derivation of parameters for binary oxides and their use in ternary oxides. *Physica B + C* **1985**, *131*, 114–118. [[CrossRef](#)]
56. Gale, J.D. Empirical potential derivation for ionic materials. *Philos. Mag. B* **1996**, *73*, 3–19. [[CrossRef](#)]
57. Guo, Q.; Zhao, Y.; Jiang, C.; Mao, W.L.; Wang, Z.; Zhang, J.; Wang, Y. Pressure-induced cubic to monoclinic phase transformation in erbium sesquioxide Er₂O₃. *Inorg. Chem.* **2007**, *46*, 6164–6169. [[CrossRef](#)] [[PubMed](#)]
58. Berard, M.F.; Wilder, D.R. Cation Self-Diffusion in Polycrystalline Y₂O₃ and Er₂O₃. *J. Am. Ceram. Soc.* **1969**, *52*, 85–88. [[CrossRef](#)]
59. Sharif, A.A.; Chu, F.; Misra, A.; Mitchell, T.E.; Petrovic, J.J. Elastic Constants of Erbia Single Crystals. *J. Am. Ceram. Soc.* **2004**, *88*, 2246–2250. [[CrossRef](#)]

60. Baur, W.H. The geometry of polyhedral distortions. Predictive relationships for the phosphate group. *Acta Cryst. B* **1974**, *30*, 1195–1215. [[CrossRef](#)]
61. Ertl, A.; Hughes, J.M.; Pertlik, F.; Foit, F.F.; Wright, S.E.; Brandstatter, F.; Marler, B. Polyhedron Distortions in Tourmaline. *Can. Mineral.* **2002**, *40*, 153–162. [[CrossRef](#)]
62. Hehlen, M.P.; Brik, M.G.; Krämer, K.W. 50th anniversary of the Judd-Ofelt theory: An experimentalist's view of the formalism and its application. *J. Lumin.* **2013**, *136*, 221–239. [[CrossRef](#)]

Disclaimer/Publisher's Note: The statements, opinions and data contained in all publications are solely those of the individual author(s) and contributor(s) and not of MDPI and/or the editor(s). MDPI and/or the editor(s) disclaim responsibility for any injury to people or property resulting from any ideas, methods, instructions or products referred to in the content.